

Computed SAR and Thermal Elevation in a 0.25mm 2D Model of the Human Eye and Head in response to an Implanted Retinal Stimulator. Part I: Models and Methods

Stephen C. DeMarco, Gianluca Lazzi, *Senior Member, IEEE*, Wentai Liu, *Senior Member, IEEE*, James D. Weiland, *Member, IEEE*, and Mark S. Humayun, *Member, IEEE*

Abstract—Retinitis pigmentosa and age-related macular degeneration lead to blindness through progressive loss of retinal photoreceptors. Attempts are underway to construct a visual prosthesis to recover a limited sense of vision for these patients with the aid of implantable electronic devices. The function of these microchips is to provide electrical stimulation to existing viable retinal tissues -living ganglion and bipolar cells-, using an array of on-chip stimulus circuits, while the dominant mechanism for power and data communication for these implanted devices has been wireless inductive telemetry using coils.

This paper describes methods and models used to estimate the heating induced in the human eye and surrounding head tissues subject to the operation of this retinal prosthesis. A two-dimensional 0.25mm high-resolution human head model has been developed with the aid of a new semi-automatic graphical segmentation algorithm. Finite-Difference based numerical methods for both electromagnetic and thermal modeling have been used to determine the influence of the Specific Absorption Rate (SAR) (associated with 2MHz inductive coupling to the implant) and of stimulator Integrated Circuit (IC) power on tissue heating under different operational conditions and different hypothesis on choroidal blood flow and thermal conductivity of the complex implanted circuitry.

Results, provided in Part II of this paper, show that temperature increase of approximately 0.6°C and 0.4°C are induced in the human eye in the absence and presence of choroidal blood flow, respectively, when a 60-electrode retinal prosthesis is operating in the worst-case scenario. Correspondent temperature rises of approximately 0.19°C and 0.004°C on the retina are obtained for these cases. Comparison with *in vivo* experimental measurements on intraocular heating in dog eyes shows good agreement.

Index Terms—Retinitis-Pigmentosa, Age-Related Macular Degeneration, Retina-Prosthesis, FDTD, SAR, Temperature, Thermal-Simulation, Stimulator-IC

I. INTRODUCTION

Age Related Macular Degeneration (AMD) and Retinitis Pigmentosa (RP), among the leading causes of blindness[1], affect over 10 million people worldwide through progressive photoreceptor loss (rod/cones) in the retina[2], [3]. The photoreceptor cells in a healthy retina initiate a neural signal in response to incident light. This neural signal is further processed by bipolar and ganglion cells of the inner retina prior to delivery to higher visual processing areas in the cortex. Retinal photoreceptors are almost completely absent in the retina of end-stage RP and AMD patients, while the bipolar cell and ganglion cells,

S.C. DeMarco, G. Lazzi, and W. Liu are with the Dept. of Electrical and Computer Engineering, NC State University, Raleigh, North Carolina, USA. The Work of G. Lazzi is supported in part by the Whitaker Foundation under contract RG-00-0298 and in part by NSF CAREER award number ECS-0091599. The work of W. Liu is supported in part by NSF award number BES-9808040 and in part by NIH.

J. D. Weiland and M.S. Humayun are with the Doheny Eye Institute at the University of Southern California, Los Angeles, California, USA. The work J.D. Weiland and M.S. Humayun is supported in part by NSF award BES-9810914 and in part by NIH.

through which the photoreceptors normally synapse, may survive at higher rates[4], [5]. The ganglion and bipolar cells remain intact, and due to the anatomy of the retina, they are in a position where they may respond to artificially-induced electrical stimulation via an implant. The demonstration that direct electrical stimulation of retinal ganglion cells can create visual sensation in patients has been shown clinically[6], [7]. Patients have been able to recognize English characters and other simple forms when stimulated by a small array of retinal electrodes. This opens the possibility of an electronic prosthesis to bypass the defective photoreceptors.

A conceptual schematic of the retinal prosthesis system is given in Figure 1. It consists of two units, extra-ocular and intra-ocular. The extra-ocular unit includes a camera for the collection of images, a data encoding chip for the discretization of the image in a 8x8 pixelized data-set, and a telemetry coil for the transmission of power and data to the intra-ocular unit. The latter unit consists of a receiving telemetry coil, power and signal transceiver and processing chip, a stimulation current driver, and a stimulating electrode array mounted on the retina. The the 5.5mm×5.25mm stimulator chip occupies a central position within the eyeball so as to better isolate its heat and mechanical stresses from the sensitive retina, while the stimulus currents are delivered to the retinal surface via the electrode array.

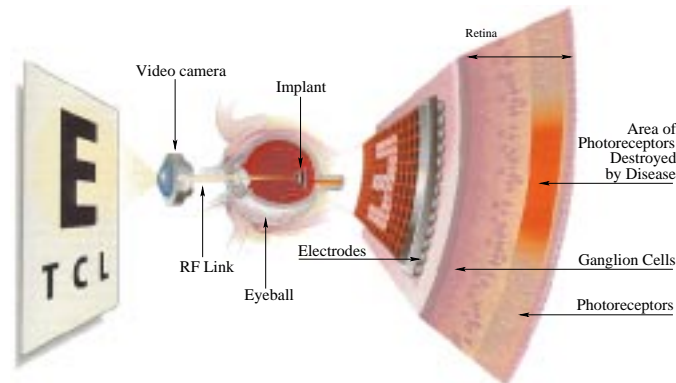


Fig. 1. Block diagram for the retina prosthesis system

As with all implantable electronic devices, the operation of the retinal prosthesis implanted in a human patient is expected to bring about an increase in the natural steady state temperature of the eye and surrounding head tissues. Therefore, a study is undertaken via numerical simulation to predict the extent of

temperature increase due to the operation of the retinal prosthesis. Ocular heating is being accounted for in terms of inductive powering (for which we quantify the specific absorption rate of electromagnetic power deposition) and the power dissipation in an implantable retinal stimulator microchip positioned at mid-vitreous. Although the prosthesis will consist of additional components including the receiving coil and mechanical support structures, our thermal studies are limited at this time to the SAR associated with inductive coupling and the power consumption in the implanted chip itself.

In recent years, studies and results have been reported in which the temperature increases in the head are of interest. Many of these have been brought about from the proliferation of cellular phones and concerns of their influence on the human head [8], [9], [10]. Furthermore, supposed links between electromagnetic exposure and the formation of cataracts [11], [12] has led to increased interest in studies of thermal heating in the human eye due to radiation in wireless computer networks [13], from infrared radiation in industrial settings [14], and to forms of electromagnetic exposure [15]. These studies have been primarily conducted at frequencies in the vicinity of 700Mhz to 2.45Ghz, due to the proliferation of wireless devices operating in these bands.

In this paper we describe methods and models used to compute estimates of heating in the human eye and surrounding head tissues subjected to the operation of such a retinal prosthesis. Electromagnetic power deposition resulting from inductive telemetry and power dissipation from the implanted stimulator IC are the heating mechanisms which are characterized.

The paper is organized into seven major sections. A review of the numerical FDTD and thermal methods is presented in Section II, accompanied by a validation of the numerical methods against analytical derivations. Section III offers comments on scaling considerations for modeling \vec{E}/\vec{H} -field distribution from the three dimensional transmitter coil in two dimensional simulation. The mathematical modeling of power dissipation in the stimulator IC for use in the numerical thermal method is formulated in Section IV and computed in Section V. A discussion of human head and eye model generation and the properties of the biological tissues is provided in Section VI and Section VII, respectively. The SAR and thermal simulation results are presented in Part II of this paper, along with validation according to measured data from physical thermal experiments.

II. COMPUTATIONAL METHODS

In order to reduce the computational complexity, the amount of required memory, and the simulation time, simulations of electromagnetic deposition and thermal elevation in the human head are conducted in two dimensions. In fact, it is possible to approximate the fields generated by the three dimensional transmitter coil used for inductive telemetry (as in the head/eye simulations for the retinal prosthesis) *via* two sources of opposite polarity normal to a plane passing through the center of the coil and coplanar with the coil axis.

A two-dimensional *D-H* Transverse Magnetic (TM) formulation of the Finite-Difference Time-Domain (FDTD) method has been used to compute the induced electromagnetic energy in a 0.25 mm resolution head model derived from the visible man

project (see Section VI). This *D-H* formulation has the advantage that the Perfectly Matched Layer (PML) absorbing boundary conditions are independent from the background dielectric materials in the FDTD mesh (both in 2D and 3D formulations), thus allowing the truncation of the head model as described in [16] in order to limit the computational space. The development of the method closely parallels that in [16] and [17], and in the sake of brevity will not be repeated here.

The thermal elevation in biological tissue can be computed by means of the bio-heat conduction equation [13] which includes the heating effect of basal metabolism, A_0 , and the cooling effect of blood perfusion, B , in the tissues. For tissue which is irradiated electromagnetically, the bioheat equation is further expanded to account for the heating effect of specific absorption rate, SAR , which is a measure of absorbed power per unit mass of tissue due to exposure to electromagnetic fields, and is expressed as $SAR = \frac{\sigma \|\vec{E}\|^2}{2\rho}$ in $\left[\frac{W}{kg}\right]$, for conductivity, σ , electric field, \vec{E} , and mass density, ρ . Furthermore, the dissipated power of the implanted stimulator IC, $P_{chip(3D)}$, is also expected to raise tissue temperature, and is included as a power density in the continuous space with units of $\left[\frac{W}{m^3}\right]$. The resulting expanded *bio-heat* equation is given as:

$$C\rho \frac{\partial T}{\partial t} = K\nabla^2 T + A_0 - B(T - T_b) + \rho SAR + P_{chip(3D)}^{(density)} \quad \left[\frac{W}{m^3}\right]_{(continuous)} \quad (1)$$

where $K\nabla^2 T$ is the thermal spatial diffusion term¹, for Celsius temperature, T , thermal conductivity, K , specific heat, C , mass density, ρ , and blood temperature, T_b , assumed constant at 37°C.

At the boundary of the tissue where the surrounding environment is encountered, the conduction of heat through the tissue arriving at the boundary normal to the surface must match the convective transfer of heat into the environment [13]. The exchange of heat with the surrounding environment is proportional to the difference between the surface temperature and the environmental temperature [8], [13] as given in Equation 2:

$$K \frac{\partial T}{\partial n}(x, y, z) = -H_a(T_{(x,y,z)} - T_a) \quad \left[\frac{W}{m^2}\right] \quad (2)$$

where $T_{(x,y,z)}$ is evaluated on the surface, n is the surface normal, H_a is the convection coefficient for heat exchange with the environmental ambient temperature with a value of $20 \frac{J}{m^2 s ^\circ C}$ [13], and T_a is the surrounding ambient temperature, assumed constant at 24°C. Based on the derivation from [13], Equation 1 and Equation 2 are spatially/temporally discretized and combined as in Equation 3 for simulation on the 2D head/eye model, developed in section VI. In particular, the SAR and stimulator

¹ A number of two- and three-dimensional numerical tests of the chip model positioned in the center of a cylinder or a sphere have shown that the use of the simplified thermal diffusion term $K\nabla^2 T$ in lieu of the more generalized $\nabla(K\nabla T)$ term in the two-dimensional modeling of the implanted microchip provides results that are in better agreement with those obtained by three-dimensional simulations employing the generalized term $\nabla(K\nabla T)$.

IC power dissipation density are now expressed as 2D quantities in the discretized space.

$$\begin{aligned}
 T_{(i,j)}^{n+1} = & \frac{K\delta t}{\rho C\delta x^2} \left(T_{(i-1,j)}^n + T_{(i+1,j)}^n + T_{(i,j-1)}^n + T_{(i,j+1)}^n \right) + \\
 & \frac{\delta t}{\rho C} \left[\rho SAR_{(i,j)} + P_{chip(2D)}^{(density)}(i,j) + A_{0(i,j)} + B_{(i,j)}T_b \right] + \\
 & T_{(i,j)}^n \left[1 - \left(N_{INT} \frac{K}{\rho C\delta x^2} + N_{EXT} \frac{H}{\rho C\delta x} + \frac{B}{\rho C} \right) \delta t \right] + \\
 & N_{EXT} \frac{H\delta t T_a}{\rho C\delta x} \quad [^\circ\text{C}]
 \end{aligned} \quad (3)$$

where N_{INT} is the number of interior points adjacent to cell (i, j) and N_{EXT} is the number of exterior points adjacent to cell (i, j) (ie- those outside of the model and belonging to the surrounding environment). The maximum time step to ensure stability of the algorithm is considered as the minimum value of the expression of Equation 4 [13], evaluated for all tissues and materials present in the discretized head/eye model.

$$\delta t \leq \min_{m \in M} \left(\frac{1}{\frac{N_{INT}K_m}{\rho_m C_m \delta x^2} + \frac{N_{EXT}H}{\rho_m C_m \delta x} + \frac{B_m}{\rho_m C_m}} \right), \quad \text{where } M \text{ is the set of tissues} \quad (4)$$

Equations 3–4 are used to calculate the temperature rise in the eye when exposed to electromagnetic radiation from inductive coupling and to power dissipation from the implanted stimulator microchip. The parameters used in these equations together with their units are summarized in table I.

TABLE I
PARAMETERS OF THE DISCRETIZED BIO-HEAT EQUATION

Symbol	Physical Property	Units
T	Temperature	$^\circ\text{C}$
t	continuous time	s
n	surface normal	–
ρ	mass density	$\frac{\text{kg}}{\text{m}^3}$
C	specific heat	$\frac{\text{J}}{\text{kg} \cdot ^\circ\text{C}}$
K	thermal conductivity	$\frac{\text{J}}{\text{m} \cdot \text{s} \cdot ^\circ\text{C}}$
H_a	convective transfer coefficient (for ambient environment temperature)	$\frac{\text{J}}{\text{m}^2 \cdot \text{s} \cdot ^\circ\text{C}}$
A_0	basal metabolic rate	$\frac{\text{J}}{\text{m}^3 \cdot \text{s}}$
B	blood perfusion coefficient	$\frac{\text{J}}{\text{m}^3 \cdot \text{s} \cdot ^\circ\text{C}}$
T_b	blood temperature (constant)	$^\circ\text{C}$
T_a	environment (ambient) temperature (constant)	$^\circ\text{C}$
δx	spatial step (resolution) in the x, i direction	m
δy	spatial step (resolution) in the y, j direction	m
δz	spatial step (resolution) in the z, k direction	m
δt	discretized time step	s
SAR	specific absorption rate	$\frac{\text{W}}{\text{kg}}$
$P_{chip(2D)}^{(density)}(i, j)$ (discrete)	2D power dissipation density	$\frac{\text{W}}{\text{m}^3}$
$P_{chip(3D)}$	stimulator IC power dissipation in 3D	W

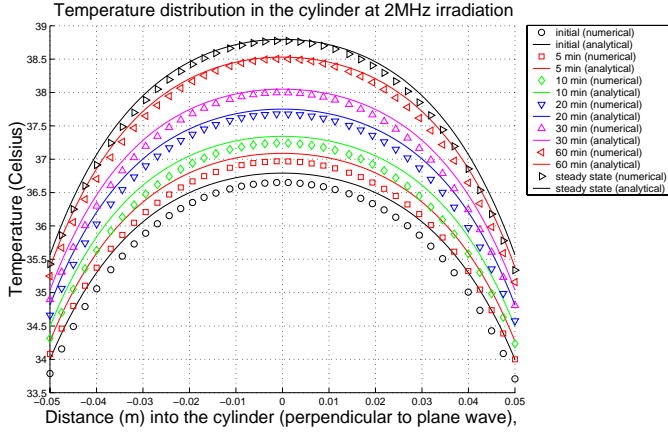
The accuracy of the implemented methods has been verified against the analytical solution for the specific absorption rate and the thermal response associated with a plane wave impacting a solid lossy cylinder, derived in [18]. The validation of our FDTD and thermal implementations is performed at the frequency of 2.45GHz reported in [18] in order to compare with the published results as well as at 2MHz, which is the operating frequency of the extra-ocular transmitting coil used to inductively power the implanted micro-stimulator. An excellent agreement between numerical and analytical results is obtained for both frequencies. Figure 2a shows analytical and numerically computed temperature in a 10cm diameter cylinder exposed to a plane wave of power density $10 \frac{\text{mW}}{\text{cm}^2}$ at the frequency of 2MHz. The curves report the temperature at various time intervals subsequent to the initial irradiation time, along the diameter of the cylinder which is perpendicular to the direction of propagation of the incident plane wave. The computed two-dimensional pattern is shown in Figure 2b.

III. MODELING OF THE EXTRA-OCULAR COIL

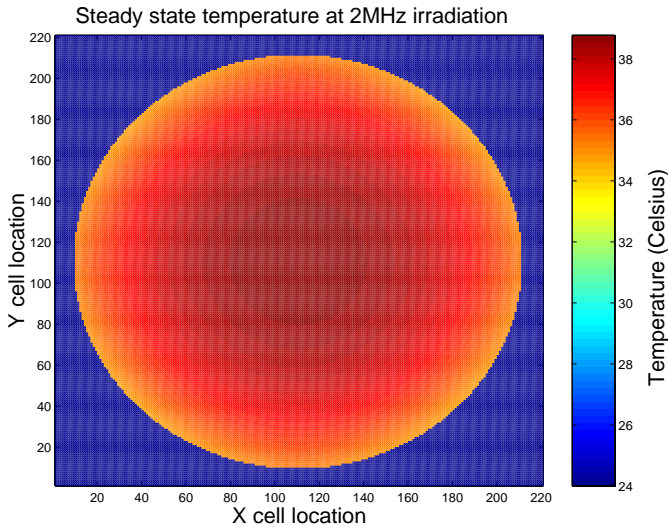
As the simulations of temperature increase in the head/eye model developed here are conducted in two dimensions, special treatment is required for the transmitter coil. The current version of the telemetry system includes an extra-ocular transmitting multi-turn coil of diameter two inches located at a distance of approximately 2cm from the human eye, and an intra-ocular receiving multi-turn coil of diameter 7mm that replaces the human lens. The extra-ocular coil needs to carry a current of 2A to deliver the necessary power to the intra-ocular unit.

For a low-frequency three dimensional coil of radius, R , and turns count, N , carrying a current of I , the magnetic field \vec{H} is given by $\|\vec{H}\| = \frac{NI}{2R}$. The coil current in a three dimensional model space would be approximated with a finite number of tangential current vectors positioned around the circumference of the coil. However, for performing two-dimensional simulations, the coil current is represented with two parallel and tangential current vectors of opposite polarity.

This approximation requires that the theoretical value of \vec{H} at the center of the multi-turn external coil in the 2D sense be scaled to that of the magnetic field at the center of the real, three-dimensional, coil model. Even though the two and three-dimensional cases are characterized by different rates of decay of the electromagnetic field, we have verified that, given the coil dimensions and its distance from the surface of the eye, the two-dimensional field approximation closely parallels the three-dimensional one within the eye region. We have verified both numerically and analytically that the two-dimensional equivalent coil represents the worst-case scenario, in the sense that the fields induced in the eye and head computed by the two-dimensional radiating model are generally higher than the corresponding fields computed by the three-dimensional one. This has been verified by means of two- and three-dimensional FDTD simulations as well as by comparing analytical solutions of the electromagnetic fields generated in free space by the two- and three-dimensional approximations of the radiating device [19].



(a) Comparison of analytically and numerically computed temperature



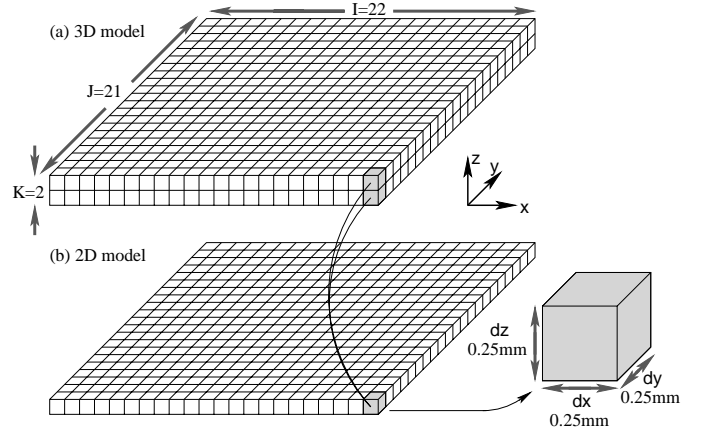
(b) Numerically computed temperature distribution

Fig. 2. Temperature distribution in the test cylinder at 2MHz irradiation

IV. MODELING POWER DISSIPATION IN THE STIMULATOR IC

Modeling of the stimulator microchip also requires approximations that allow us to correctly represent the power dissipated by the chip in a two-dimensional space, rather than three-dimensional. MOSIS reports the die size for our *Retina-3.5* stimulator IC [20] in the AMI-1.2 μm process as 4.7mm \times 4.6mm \times 500 μm . However, after accounting for clearance around the pad-ring for the wafer dicing saw, the die size becomes 5.53mm \times 5.25mm \times 508 μm .

Discretizing this chip volume to 0.25mm spatial resolution, yields the 3D chip model shown in Figure 3a with cellular dimensions $I = 22 \times J = 21 \times K = 2$, with the total power dissipation expressed as a volume summation of the discrete power density, $P_{chip(3D)}^{(density)}(i, j, k)$, as given in Equation 5.

Fig. 3. *Retina-3.5* stimulator IC models discretized to 0.25mm uniform spatial resolution

$$P_{chip(3D)} = \sum_{i=1}^I \sum_{j=1}^J \sum_{k=1}^K P_{chip(3D)}^{(density)}(i, j, k) \quad (5)$$

When considering a 2D model of the 3D stimulator chip for thermal simulation in the 2D head/eye model of Figure 8, the total power, $P_{chip(3D)}^{(density)}$, is retained by integrating (or summing) the power density for the 3D chip model along the k -axis for each cell (i, j) in the 2D chip model. Although this yields power density units in 2D of $\left[\frac{\text{W}}{\text{m}^2}\right]$ we consider that the 2D model shown in Figure 3b can be conceptually extended infinitely in the k -dimension. Therefore units of $\left[\frac{\text{W}}{\text{m}^3}\right]$ are retained in the 2D chip model for the power density at (i, j) consistent with the units of the tissue properties, such as mass density ρ in $\left[\frac{\text{kg}}{\text{m}^3}\right]$. This means of condensing the power density is formulated as:

$$P_{chip(2D)}^{(density)}(i, j) = \sum_{k=1}^K P_{chip(3D)}^{(density)}(i, j, k) \quad (6)$$

In general the power density varies across a chip, but in the case of our *Retina-3.5* stimulator, the IC [20] consists of an array of 60 identical stimulus current driver circuits which are uniformly distributed over 75% of the chip area (25% is occupied by digital control circuits). Thus, we approximate the power density as uniformly distributed, such that

$$P_{chip(2D)}^{(density)}(i, j) = \sum_{k=1}^K \frac{P_{chip(3D)}}{(I dx)(J dy)(K dz)}, \quad (7)$$

where $dx = dy = dz = 0.25\text{mm}$, and $I = 22$, $J = 21$, and $K = 2$. The power density, $P_{chip(2D)}^{(density)}(i, j)$, as defined here and associated with the 2D chip model of Figure 3b, is the same value used in the 2D bio-heat formulation of Equation 3.

V. COMPUTING POWER DISSIPATION IN THE STIMULATOR IC

The sixty stimulus circuits of our *Retina-3.5* stimulator IC [20] provide biphasic current outputs for retinal stimulation,

with programmable amplitudes, pulse widths, and pulse rate. The power consumption associated with operating the micro-stimulator can be accounted for in terms of the power dissipated in the retinal tissue (the *load*) plus additional power overhead required by the micro-stimulator IC. This is expressed in Equation 8 for instantaneous power as a function of time, where the superscript “60” in parentheses refers to the case where all sixty stimulation channels are active. The subscripts *chip*, *load*, and *consumed* refer to the power consumed in the micro-stimulator, retinal-tissue, and of the combined system, respectively.

$$P_{consumed}^{(60)}(t) = P_{chip}^{(60)}(t) + P_{load}^{(60)}(t) \quad (8)$$

A. Simulated power dissipation in the stimulator IC

Since the *Retina-3.5* stimulator IC [20] layout contains nearly 70000 FETs, circuit simulators such as *Hspice* cannot practically conduct chip level simulations which cover milliseconds of real time. However, the array of stimulus circuits accounts for the majority of the area on our IC (about 75%). Therefore, a reasonable estimate of the dissipated power of the chip can be formulated from a simulation of a single output driver (one from the array of sixty), the biasing circuit (which manifests static power dissipation), and the digital section (associated with packet synchronization and timing generation), designated as subcircuits, X1, X2, and X3, respectively as illustrated in Figure 4.

In simulation, the output driver of subcircuit X1 is loaded with a resistance $R_{load} = 10k\Omega$ to model retinal impedance [21]. The power dissipation of the chip could be predicted from the simulated estimates of subcircuits X1 – X3, designated $P_{X1} - P_{X3}$ as in Equation 9, excluding the power, P_{load} , dissipated in R_{load} which is off chip.

$$P_{chip(3D)} = P_{chip}^{(60)} = 60(P_{X1}) + P_{X2} + P_{X3} \quad (9)$$

In simulating the power requirements of the stimulator IC, the standard biphasic current pulse for retinal stimulation is considered as reported in [7] and shown in Figure 5. The micro-stimulator is programmed to produce this current waveform on all sixty output channels simultaneously. Equal anodic and cathodic currents of $400\mu A$ (the typical case) and $600\mu A$ (the worse or maximum case) for *Retina-3.5* are considered, with V_{dd} and V_{ss} set at $+5v/-5v$ or $+7v/-7v$ for each case, respectively, as appropriate[7]. Pulse repetition rates of 50Hz and 60Hz are considered in keeping with results of flicker fusion experiments reported in [7]. Anodic and cathodic pulse widths and interphase delay were kept equal and varied among 1ms, 2ms, and 3ms, consistent with stimulation experiments also reported in [7].

These parameters are annotated as A , W , and, T on the stimulus waveform of Figure 5 representing current amplitude, pulse and interphase-delay width, and period, respectively.

The subcircuits of Figure 4 were programmed to produce the biphasic stimulus pulse of Figure 5 in each of the parametric combinations described (twelve cases in all). Subsequently, *Hspice* simulations were conducted to estimate the power dissipation of *Retina-3.5* when operating in each case. The results are tabulated in Table II.

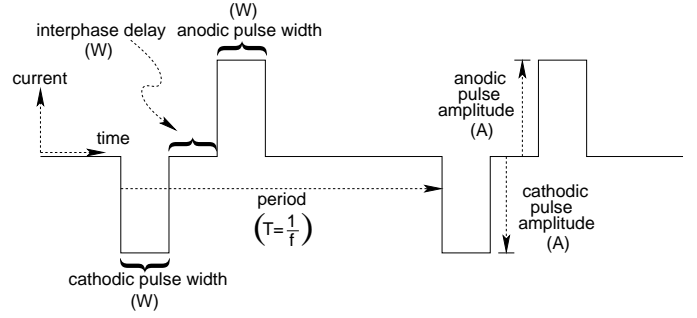


Fig. 5. Parameters of the biphasic current pulse used for retinal stimulation

When computing power estimates on semiconductor circuits *Hspice* considers only the power lost, or dissipated. Therefore, the estimates of $P_{chip}^{(60)}$ from Table II are taken as losses which would give rise to heat, and are subsequently used for $P_{chip(3D)}$ in Equation 7 to compute $P_{chip(2D)}^{(density)}$ (i, j) for the thermal method in Equation 3 to predict temperature increase in the 2D head/eye model.

B. Experimental validation of power consumption and dissipation in the stimulator IC

Experimental measurements of the microchip power consumption were taken to validate the *Hspice* simulations of the IC layout. Recall that our stimulator IC operates from dual DC supply rails of V_{dd} and V_{ss} to produce the anodic and cathodic phases, respectively, with respect to a central ground return, *Gnd*. Therefore, an experimental estimate of chip power can be inferred from a measurement of the power consumption minus power dissipation in the 60 loads, as in Equation 10

$$P_{consumed}^{(60)} = V_{dd}I_{dd}^{(60)} + V_{ss}I_{ss}^{(60)} - 60 \frac{(V_{load})^2}{R_{load}} \quad (10)$$

where I_{dd} and I_{ss} are the average supply currents for the V_{dd} and V_{ss} supplies and V_{load} is the RMS voltage measured across the load resistance, $R_{load} = 10k\Omega$. Results of the measurement experiment along with the inferred micro-stimulator power are summarized in Table III. A comparison between the simulated and measured estimates for the chip power is included. The difference between the simulated and experimental estimates of the power dissipation vary by no more than about 2mW, thus indicating that the experimental measurement is in good agreement with the simulated estimates.

VI. HEAD AND EYE COMPUTATIONAL MODELS

Since the determination of a detailed thermal distribution in the human eye is critical for the development of a safe retinal prosthesis implant, there is the need to develop a high-resolution two-dimensional head model which accurately accounts for all the anatomical features of the human eye. Since there are no available Magnetic Resonance Images (MRI) accurate enough to capture the finest anatomical details of the human eye, it has been necessary to derive the eye model from an anatomically accurate sketch of a human eye, taken from [22],[23].

TABLE II

Hspice SIMULATED POWER DISSIPATION FOR OUR *Retina-3.5* IC RESULTING FROM VARIATIONS IN BIPHASIC STIMULUS

V_{dd}, V_{ss} [V _{DC}]	current A [μ A]	frame rate ² $f = \frac{1}{T}$ [Hz]	pulse width ³ W [ms]	bias power P_{X1} [mW]	driver power P_{X2} [mW]	load power P_{load} [mW]	driver power $\times 60$ $P_{X2} \times 60$ [mW]	load power $\times 60$ $P_{load} \times 60$ [mW]	digital power P_{X3} [mW]	chip power ⁴ $P_{chip}^{(60)}$ [mW]
+5, -5	400 ¹	50	1	2.4700	0.1041	0.1633	6.2436	9.8004	0.4726	9.1862
+5, -5	400 ¹	50	2	2.4700	0.2036	0.3251	12.2154	19.5066	0.4726	15.1580
+5, -5	400 ¹	50	3	2.4700	0.3041	0.4884	18.2448	29.3070	0.4726	21.1874
+5, -5	400 ¹	60	1	2.4700	0.1243	0.1951	7.4562	11.7030	0.4750	10.4012
+5, -5	400 ¹	60	2	2.4700	0.2443	0.3901	14.6568	23.4066	0.4750	17.6018
+5, -5	400 ¹	60	3	2.4700	0.3643	0.5852	21.8568	35.1102	0.4750	24.8018
+7, -7	600 ²	50	1	3.5647	0.2043	0.3310	12.2604	19.8618	0.4964	16.3216
+7, -7	600 ²	50	2	3.5647	0.3962	0.6589	23.7696	39.5310	0.4964	27.8308
+7, -7	600 ²	50	3	3.5647	0.5899	0.9899	35.3916	59.3928	0.4964	39.4527
+7, -7	600 ²	60	1	3.5647	0.2441	0.3953	14.6448	23.7174	0.5017	18.7112
+7, -7	600 ²	60	2	3.5647	0.4754	0.7906	28.5228	47.4354	0.5017	32.5892
+7, -7	600 ²	60	3	3.5647	0.7067	1.1859	42.4008	71.1540	0.5017	46.4672

¹Anodic and cathodic pulse amplitudes resulting from *Hspice* simulation at $V_{dd} = +5$ v and $V_{ss} = -5$ v were $+400.8\mu$ A and -405.1μ A, respectively.

²Anodic and cathodic pulse amplitudes resulting from *Hspice* simulation at $V_{dd} = +7$ v and $V_{ss} = -7$ v were $+575.3\mu$ A and -572.1μ A, respectively. The driver output stages on the stimulator IC transition from saturation to the linear region when attempting to provide 600μ A for $R_{load} = 10$ k Ω [21] with $V_{dd} = +7$ v and $V_{ss} = -7$ v. Therefore, actual currents fall short of the requested values.

²Actual frame rates are 49.827Hz and 60.048Hz, derived from a 12MHz oscillator on the extra-ocular communications processor, which controls stimulus timing.

³Actual pulse widths are 1.023ms, 2.046ms, and 2.991ms for 50Hz frame rate and 1.045ms, 2.025ms, and 3.004ms for 60Hz frame rate again derived from the 12MHz oscillator.

⁴Excludes load power.

TABLE III

EXPERIMENTALLY MEASURED POWER CONSUMPTION AND DISSIPATION IN OUR *Retina-3.5* IC RESULTING FROM VARIATIONS IN BIPHASIC STIMULUS

V_{dd}, V_{ss} ¹ [V _{DC}]	current ² A [μ A]	frame rate $f = \frac{1}{T}$ [Hz]	pulse width W [ms]	measured consumption ³ $P_{consumed}^{(60)}$ [mW]	measured load power $P_{load}^{(60)}$ [mW]	inferred chip power ⁴ $P_{chip}^{(60)}$ [mW]	simulated chip power ⁵ $P_{chip}^{(60)}$ [mW]
+5, -5	400	50	1 ⁴	18.4818	11.3276	7.1541	9.1862
+5, -5	400	50	2 ⁴	36.4597	20.8378	15.6219	15.1580
+5, -5	400	50	3 ⁴	53.0817	28.7304	24.3513	21.1874
+5, -5	400	60	1 ⁵	22.4489	11.6612	10.7877	10.4012
+5, -5	400	60	2 ⁵	42.7871	22.8569	19.9302	17.6018
+5, -5	400	60	3 ⁵	61.2672	33.6595	27.6076	24.8018

¹Due to limitations in the current fabrication of our *Retina-3.5* stimulator IC, operation at $V_{dd} = +7$ v, $V_{ss} = -7$ v yields an amplitude imbalance measured between anodic and cathodic current when programmed to match. Therefore, experimentally measured power consumption and dissipation for validation with the simulated data of Table II were conducted only for the cases of $V_{dd} = +5$ v, $V_{ss} = -5$ v, which the matching is acceptable.

²Anodic and cathodic pulse amplitudes measured experimentally at $V_{dd} = +5$ v and $V_{ss} = -5$ v were 400μ A and -408μ A, respectively.

³The resistance R_{series} placed in series with the power rails to facilitate experimental measurement of supply currents, I_{dd} and I_{ss} , is taken at a low value of 10.3 Ω . Therefore, the associated power dissipations, $\frac{(\Delta V_{dd})^2}{R_{series}}$ and $\frac{(\Delta V_{ss})^2}{R_{series}}$, are negligible and therefore not included in these measurements.

⁴Inferred from $P_{chip}^{(60)} = P_{consumed}^{(60)} - P_{load}^{(60)}$, which measures the difference in power consumed from the supplies and power dissipated in the 10k Ω resistive loads when all 60 output drivers are active.

⁵Duplicated from Table II.

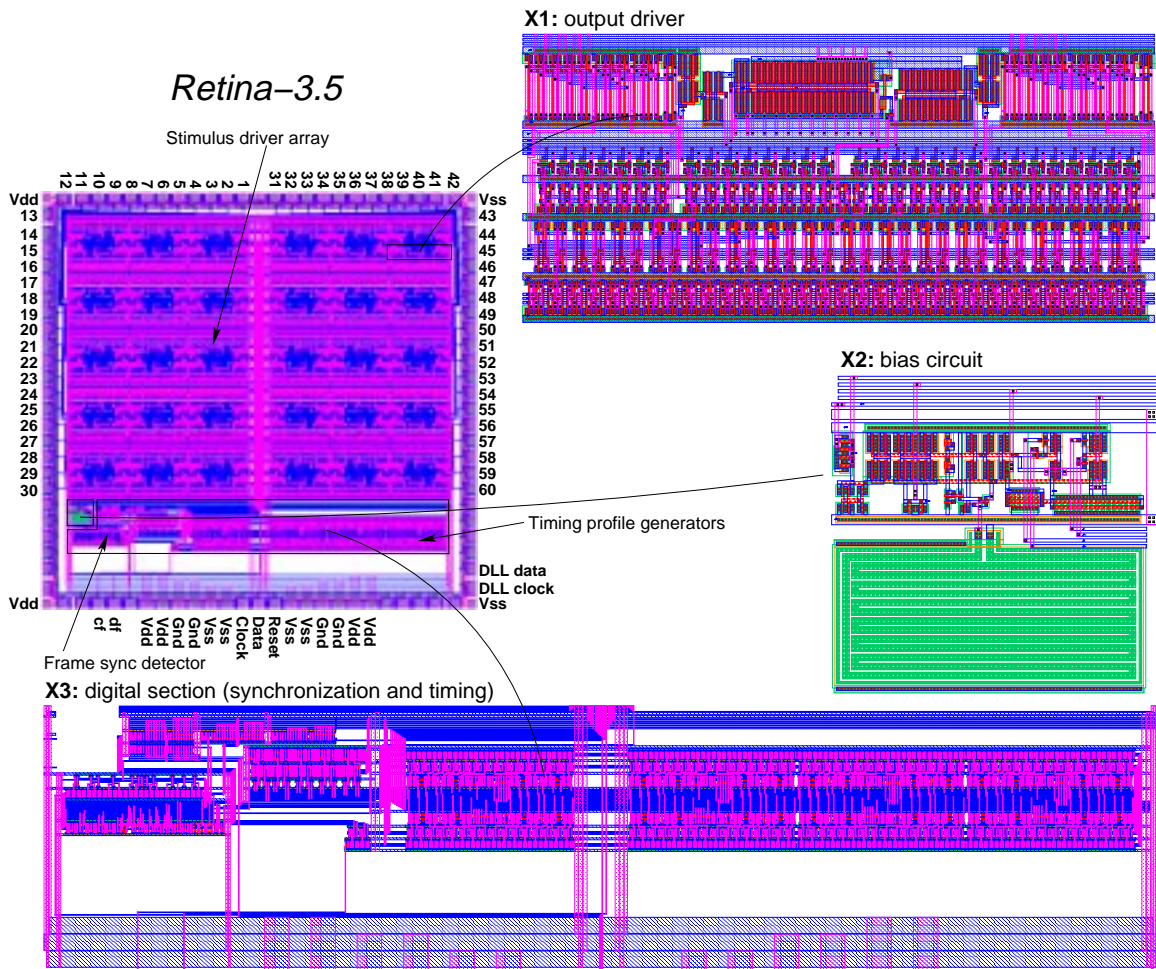


Fig. 4. Retina-3.5 stimulator IC layouts simulated in Hspice to determine power dissipation

The sketch of the eye was electronically scanned to obtain an image of roughly 600×600 pixel resolution. Subsequently, the optic nerve and the muscles connecting to the sclera were removed, and the resulting image was color segmented according to the distinct tissues represented, as shown in Figure 6a.

A software application has been developed to discretize the segmented eye image onto a uniform grid of 0.25mm resolution in order to sample it to a high resolution for construction of the model. At each cell in the overlying grid, the discretizer determines the dominant tissue type occupying that cell and identifies it according to the applied color segmentation. A unique tissue identifier is assigned to each cell location which is used as an index into a table of tissues (see Table IV) specifying dielectric and thermal properties. The resulting eye model which has been discretized to a spatial resolution of 0.25mm is shown in Figure 6b.

A new two-dimensional head model was also constructed with a resolution of 0.25mm suitable for an accurate representation of the finest anatomical details of the human head. The head model is derived from an image of the human head slice at a position intersecting the eyes, taken from the National Library of Medicine (NLM) Visible Man Project [24]. As with the eye model, construction of the head model proceeds by first color segmenting the head in order that tissues may be identified by



(a) Color segmentation according to tissue type (b) 2D eye model sampled to 0.25mm using a uniform grid

Fig. 6. Discretization to obtain the 0.25mm 2D eye model

uniform color. Subsequently, the discretizer is again used to sample the head slice image to a 0.25mm model.

Since the eyes in the original head slice image from the Visible Man Project provide only two or three discernible tissues, the 0.25 mm resolution eye model separately developed is merged with the 0.25mm head model to increase ocular detail as is shown in Figure 7. A 2D silicon model of the implanted

stimulator IC of dimensions $5.5\text{mm} \times 5.25\text{mm}$ is shown at mid-vitreous in the left eye, in the position and orientation associated with implantation [25].

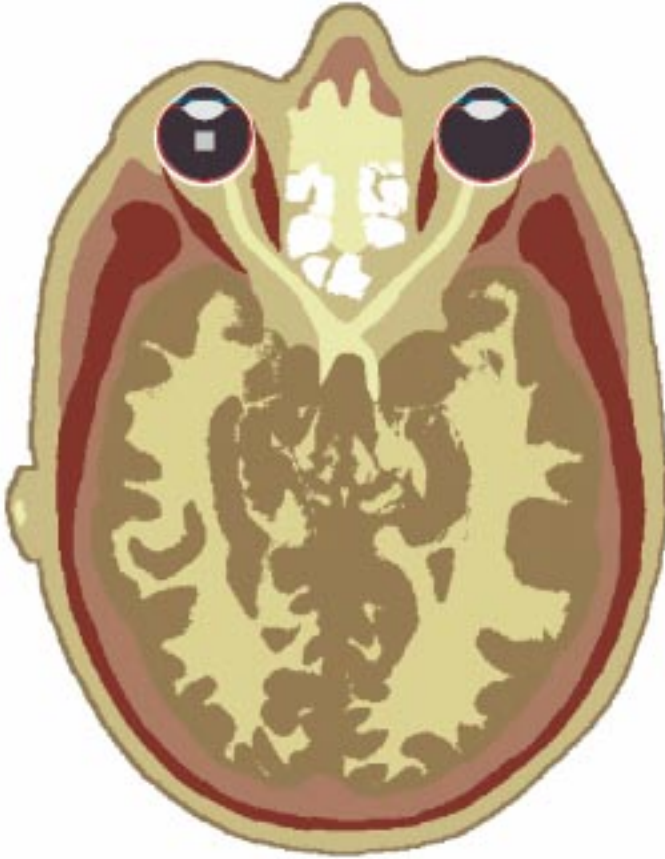


Fig. 7. Merged model of the discretized head and eye models with inclusion of the silicon stimulator IC model in the left eye

It is expected that temperature increase arising from inductive coupling and from power dissipation in the stimulator IC will be localized to the region of the eyes. Therefore, in order to decrease the required memory and simulation time, the head/eye model is truncated posterior to the eyes as shown in Figure 8.



Fig. 8. Truncated model of the merged human head/eye models

When computing Specific Absorption Rate or SAR, the posterior edge of the model is immersed in the PML layers in order to correctly support the model truncation for the reduction of the computational space, as explained in [16]. For the thermal simulation, instead, the initial steady state temperature distribution,

which is computed in the absence of any SAR and implant heating for the whole model, is forced along the posterior boundary in order to prevent inappropriate heat exchange with the surrounding environment. The model truncation is performed at a depth to which the conduction of internal heat is expected to be negligible.

VII. PHYSICAL PROPERTIES OF TISSUES

Dielectric and thermal property values have been taken from various publications collectively representing the research in electromagnetic and thermal dosimetry. The dielectric properties for the bodily tissues have been gathered from the *Dielectric Properties of Body Tissues* online database [26]. This data is compiled and organized by the *Electromagnetic Wave Research Institute of the Italian National Research Council (IROE-CNR)*, based on the work of Gabriel [27]–[31] dating back to 1996. The permittivities and conductivities are evaluated at 2Mhz corresponding to the carrier frequency of the exterior transmitter coil in the inductive powering scheme. Thermal properties and specific gravities for the biological tissues have been collected primarily from [32] released in 1990, but also from other publications [8]–[10], [13], [15], [33]–[38]. Our *Retina-3.5* stimulator IC [20] fabricated in bulk CMOS, is uniformly modeled with the physical properties of intrinsic silicon available from the online elemental database [39]. These properties used with the head/eye model are summarized in Table IV. As physical properties for some of the tissues are not explicitly available, values have been taken which match with tissues of nearest expected composition or water content.

The newly developed eye model accounts for sclera, cornea, aqueous humor, pupillary sphincter muscle, posterior chamber, crystalline lens, lens zonules, ciliary muscle, vitreous humor, choroid, and retina. Pupillary and ciliary muscles, lens zonules (likened to tendons), and muscles attached to the sclera are represented with the dielectric and thermal properties of generic human muscle. Due to its close proximity, the posterior chamber situated between the lens and pupillary muscle takes its properties from the aqueous humor. The permittivity and conductivity of the aqueous humor at 2MHz are taken as vitreous. Similarly, the mass density and thermal conductivity are shared among the aqueous and vitreous as [32] identifies a single humor for these two properties. Moreover, the specific heat properties are equal, as in [13]. The highly vascularized choroid which lies between the retina and sclera and nourishes the photoreceptors, is approximated with the physical properties of blood.

Only the dielectric properties of the retina have been found in available research literature [26]; mass density and thermal properties are not available. However, the retina is a multi-layer neural structure approximately $300\mu\text{m}$ thick with most of its composition organized as a cascade of various neuron cell types and their interconnections [22], [42], [43], [44]. Only in the innermost layer above the ganglion neurons is there a heavily axonal or nerve fiber layer. Therefore, in its composition, the retina is expected for the greater part to be analogous to brain grey matter, where there is a higher concentration of neural cell bodies and dendrites [41].

White matter represents the portion of brain neural structure

TABLE IV
DIELECTRIC AND THERMAL PROPERTIES OF TISSUES AND MATERIALS IN THE HEAD/EYE MODEL AT 2MHZ^{1,2,3}

Tissue	Relative Permittivity ϵ_R	Conductivity σ [$\frac{S}{m}$]	Mass Density ρ [$\frac{kg}{m^3}$]	Specific Heat C [$\frac{J}{kg \cdot ^\circ C}$]	Thermal Conductivity K [$\frac{J}{m \cdot s \cdot ^\circ C}$]	Blood Perfusion B [$\frac{J}{m^3 \cdot s \cdot ^\circ C}$]	Metabolic Rate (Basal) A_0 [$\frac{J}{m^3 \cdot s}$]
air	1.000	0.0000	1.16	1300	0.250	0	0
muscle	826.000	0.5476	1040	3600 ²⁰	0.498 ¹²	2700	690
deep fat	22.950	0.0255	920	2500 ²⁰	0.250 ¹³	520	180
bone	106.000 ⁴	0.0285 ⁴	1810	1300 ⁸	0.300 ¹⁴	1000	0
cartilage	815.500	0.2776	1100	3400 ²⁰	0.450 ²⁰	9100	1000
skin	858.000	0.0371	1010	3500 ²⁰	0.420 ²⁰	9100	1000
nerve	554.800	0.1556	1043 ⁹	3600 ⁹	0.503 ⁹	35000 ⁹	10000 ⁹
subcutaneous fat	22.950	0.0255	920	2500	0.250	520	180
brain grey matter	656.500	0.1807	1039 ¹⁸	3680 ¹⁸	0.565 ¹⁸	35000	10000
brain white matter	340.600	0.1118	1043 ¹⁸	3600 ¹⁸	0.503 ¹⁸	35000	10000
blood	1681.000	0.9261	1060	3840 ¹⁰	0.530 ¹⁵	—	0
sclera	1145.000	0.6889	1170	4178 ¹¹	0.580 ¹¹	0	0
scleral muscle ⁶	826.000 ⁶	0.5476 ⁶	1040 ⁶	3430 ⁶	0.498 ⁶	2700 ⁶	690 ⁶
cornea	1429.000	0.7438	1076 ¹⁸	4178 ¹¹	0.580 ¹¹	0	0
pupillary muscle ⁶	826.000 ⁶	0.5476 ⁶	1040 ⁶	3430 ⁶	0.498 ⁶	2700 ⁶	690 ⁶
post chamber ⁵	76.650 ⁵	1.5010 ⁵	1003 ⁵	3997 ⁵	0.578 ⁵	0 ⁵	0 ⁵
lens	829.700	0.4170	1100	3000 ¹¹	0.400 ¹¹	0	0
lens zonules ⁶	826.000 ⁶	0.5476 ⁶	1040 ⁶	3430 ⁶	0.498 ⁶	2700 ⁶	690 ⁶
cilliary muscle ⁶	826.000 ⁶	0.5476 ⁶	1040 ⁶	3430 ⁶	0.498 ⁶	2700 ⁶	690 ⁶
aqueous humor	76.650 ¹⁷	1.5010 ¹⁷	1003 ¹⁸	3997 ¹⁹	0.578 ¹⁸	0	0
vitreous humor	76.650	1.5010	1009 ¹⁸	3997 ¹⁹	0.594 ¹⁸	0	0
choroid ⁷	1681.000 ⁷	0.9261 ⁷	1060 ⁷	3840 ⁷	0.530 ⁷	0 ⁷	0 ⁷
retina	1145.000	0.6889	1039 ¹⁶	3680 ¹⁶	0.565 ¹⁶	35000 ¹⁶	10000 ¹⁶
silicon	— ²¹	— ²¹	2330 ²²	959 ²²	150.000 ²³	—	—

¹Dielectric properties, ϵ_R and σ , are taken from [26] unless otherwise noted

²Mass density, ρ , taken from [10] unless otherwise noted

³Blood perfusion constant, B , and basal metabolic rate, A_0 , are taken from [9] unless otherwise noted

⁴Cortical bone, taken from [26]

⁵Unavailable explicitly. Therefore, assigned the properties of aqueous humor

⁶Taken as muscle (generic)

⁷Modeled as blood

⁸Human cortical bone, taken from [32]

⁹Unavailable explicitly. Therefore, assigned the properties of brain white matter, as this is reported to have a high nerve fiber makeup and is contained in the optic nerves [40]

¹⁰Human whole blood

¹¹Taken from [13]

¹²Human skeletal muscle, taken from [32]

¹³Averaged human subcutaneous fat, taken from [32]

¹⁴Taken from [8]

¹⁵Human whole blood (43% Hct), taken from [32]

¹⁶Unavailable explicitly. Therefore, assigned the properties of brain grey matter, as this is reported to have a higher concentration of neural cell bodies and dendrites than white matter [41]

¹⁷Unavailable explicitly. Therefore, assigned the properties of Vitreous Humor

¹⁸Taken from [32]

¹⁹Taken as Humor from [13]

²⁰Taken from [9]

²¹Silicon not used in the calculation of the specific absorption rate

²²Taken from [39]

²³The thermal conductivity of the implant is dependent on the precise material composition of the stimulator IC, any additional supporting intra-ocular components, and the hermetically-sealed biocompatible casing. Therefore, thermal simulations were conducted with values of $K_{chip} \in \{10, 20, 30, \dots, 80, 90\}$, so as to characterize the dependence of temperature increase on the chip's thermal conductivity. Subsequently, in order to minimize the computational time, temperature rise associated with $K_{SI} = 150$ (corresponding to the real value of silicon) are extrapolated according to the resulting trend.

involved in communication between areas of grey matter and thus has a high nerve fiber, or axonal, composition [40]. Furthermore, as the optic nerves are reported to contain white matter [40], physical properties of nerve are assumed similar to those of white matter. Moreover, [9] and [45] report blood perfusion and basal metabolism in agreement with that of brain, or white matter. Hence, physical properties for nerve in Table IV are assigned from those explicitly available for white matter.

The thermal conductivity for the uniform silicon model of our *Retina-3.5* stimulator IC [20] was reported from [39] as

$150 \frac{J}{m \cdot s \cdot ^\circ C}$, which exceeds thermal conductivities of the bio-

logical tissues by two order of magnitude. In accordance with Equation 4, this forces a smaller time step for stability and thus a longer simulation when compared with the case where silicon is absent from the model. The thermal conductivity of the implant is dependent on the precise material composition of the stimulator IC, any additional supporting intra-ocular components, and the hermetically-sealed biocompatible casing. Therefore, thermal simulations were conducted with values of $K_{chip} \in \{10, 20, 30, \dots, 80, 90\}$, so as to characterize the dependence of temperature increase on the chip's thermal conductivity. Subsequently, in order to minimize the computational time, temperature rise associated with $K_{SI} = 150$ (corresponding to

the real value of silicon) is extrapolated according to the resulting trend.

REFERENCES

- [1] L. Hymen. "Epidemiology of eye diseases in the elderly". *Eye*, 1:330–341, 1987.
- [2] Research to prevent blindness, progress report, 1993.
- [3] Various eye care statistics, association of vision science librarians. <http://spectacle.berkeley.edu/library/stats.htm#age>, 1993.
- [4] J.L. Stone, W.E. Barlow, M.S. Humayun, E. De Juan, Jr., and A.H. Milam Jr. "Morphometric analysis of macular photoreceptor and ganglion cells in retinas with retinitis pigmentosa". *Archives of Ophthalmology*, 110:1634–1639, 1992.
- [5] A. Santos, M.S. Humayun, E. De Juan, Jr., R.J. Greenberg, M.J. Marsh, and A.H. Milam. "Inner retinal preservation in retinitis pigmentosa: a morphometric analysis". *Archives of Ophthalmology*, 115:511–515, 1997.
- [6] M.S. Humayun, E. De Juan, Jr., G. Dagnelie, R.J. Greenberg, R.H. Propst, and H. Phillips. "Visual perception elicited by electrical stimulation of the retina in blind humans". *Archives of Ophthalmology*, 114:40–46, 1996.
- [7] M.S. Humayun, E. De Juan, Jr., J.D. Weiland, G. Dagnelie, S. Katona, R. Greenberg, and S. Suzuki. "Pattern electrical stimulation of the human retina". *Vision Research*, 39:2569–2576, 1999.
- [8] J. Wang and O. Fujiwara. "FDTD computation of temperature rise in the human head for portable telephones". *IEEE Transactions on Microwave Theory and Techniques*, 47(8):1528–1534, August 1999.
- [9] P. Bernardi, M. Cavagnaro, S. Pisa, and E. Piuze. "Specific absorption rate and temperature increases in the head of a cellular-phone user". *IEEE Transactions on Microwave Theory and Techniques*, 48(7):1118–1126, July 2000.
- [10] O.P. Gandhi, G. Lazzi, and C.M. Furse. "Electromagnetic absorption in the human head and neck for mobile telephones at 835 and 1900 MHz". *IEEE Transactions on Microwave Theory and Techniques*, 44(10):1884–1897, October 1996.
- [11] A. Hirata, S.I. Matsuyama, and T. Shiozawa. "Temperature rises in the human eye exposed to EM waves in the frequency range 0.6–6 GHz". *IEEE Transactions on Electromagnetic Compatibility*, 42(4):386–393, November 2000.
- [12] A. Hirata, U. Ushio, and T. Shiozawa. "Formation of hot spots in the human eye for plane wave exposures". *Asia Pacific Microwave Conference*, 2:477–480, 1999.
- [13] P. Bernardi, M. Cavagnaro, S. Pisa, and E. Piuze. "SAR distribution and temperature increase in an anatomical model of the human eye exposed to the field radiated by the user antenna in a wireless LAN". *IEEE Transactions on Microwave Theory and Techniques*, 46(12):2074–2082, December 1998.
- [14] J.A. Scott. "The computation of temperature rises in the human eye induced by infrared radiation". *Physics in Medicine and Biology*, 33(2):243–257, 1988.
- [15] A. Taflov and M. E. Brodwin. "Computation of the electromagnetic fields and induced temperatures within a model of the microwave-irradiated human eye". *IEEE Transactions on Microwave Theory and Techniques*, MTT-23:888–896, November 1975.
- [16] G. Lazzi, O.P. Gandhi, and D. Sullivan. "Use of PML absorbing layers for the truncation of the head model in cellular telephone simulations". *IEEE Transactions on Microwave Theory and Techniques*, 48(11):2033–2039, November 2000.
- [17] D. Sullivan. *Electromagnetic Simulation Using the FDTD Method*. IEEE Press, New York, NY, 2000.
- [18] F. Bardati, G. Gerosa, and P. Lampariello. "Temperature distribution in simulated living tissues irradiated electromagnetically". *Alta Frequenza*, XLIX(2):61–67, 1980.
- [19] K.P. Esselle and M.A. Stuchly. "Neural Stimulation with Magnetic Fields: Analysis of Induced Electric Fields". *IEEE Transactions on Biomedical Engineering*, 39(7):693–700, July 1992.
- [20] S.C. DeMarco, S.M. Clements, and W. Liu. "A 60 Channel Implantable Neuro-stimulator for an Epi-Retinal Visual Prosthesis". (Unpublished).
- [21] A.B. Majji, M.S. Humayun, J.D. Weiland, S. Suzuki, S.A. D'Anna, and E. De Juan, Jr. "Long-term histological and electrophysiological results of an inactive epi-retinal electrode array implantation in dogs". *Investigative Ophthalmology and Visual Science*, 40(9):2073–2081, August 1999.
- [22] S.H. Schwartz. *Visual perception: a clinical orientation*. Appleton & Lange, Norwalk, Connecticut., 1994.
- [23] M. Salzmann. *The Anatomy and Physiology of the Human Eyeball is the Normal State*. University of Chicago Press, Chicago, Illinois, 1912. translated by Brown EVC.
- [24] The National Library of Medicine. The visible human project. http://www.nlm.nih.gov/research/visible/visible_human.html, 2000.
- [25] Personal communication with M.S. Humayun and R.J. Greenberg.
- [26] Dielectric Properties of Body Tissue: <http://safeemf.iroec.fi.cnr.it/tissprop/>.
- [27] C. Gabriel and S. Gabriel. "Compilation of the Dielectric Properties of Body Tissues at RF and Microwave Frequencies". Internet document; URL: <http://www.brooks.af.mil/AFRL/HED/hedr/reports/dielectric/home.html>.
- [28] C. Gabriel. "Compilation of the dielectric properties of body tissues at RF and microwave frequencies". Report N.AL/OE-TR- 1996-0037. Occupational and environmental health directorate, Radiofrequency Radiation Division, Brooks Air Force Base, Texas (USA), June 1996.
- [29] C. Gabriel, S. Gabriel, and E. Corthout. "The dielectric properties of biological tissues: I. Literature survey". *Physics in Medicine and Biology*, 41:2231–2249, 1996.
- [30] S. Gabriel, R.W. Lau, and C. Gabriel. "The dielectric properties of biological tissues: II. Measurements in the frequency range 10 Hz to 20 GHz". *Physics in Medicine and Biology*, 41:2251–2269, 1996.
- [31] S. Gabriel, R.W. Lau, and C. Gabriel. "The dielectric properties of biological tissues: III. Parametric models for the dielectric spectrum of tissues". *Physics in Medicine and Biology*, 41:2271–2293, 1996.
- [32] F.A. Duck. *Physical properties of tissues: a comprehensive reference book*. Academic Press, New York, NY, 1990.
- [33] C.H. Durney, H. Massoudi, and M.F. Iskander. *Radiofrequency Radiation Dosimetry Handbook*. New York, NY, 4 edition. USAF SAM-TR-85-73, USAF School of Aerospace Medicine, Aerospace Med. Div. (AFSC), Brooks Air Force Base, TX, 78235–5301, Oct. 1986.
- [34] M.A. Stuchly and S.S. Stuchly. "Dielectric Properties of biological substances—Tabulated". *Journal of Microwave Power*, 15:19–26, 1980.
- [35] J.J.W. Lagendijk. "A mathematical model to calculate temperature distributions in human and rabbit eyes during hyperthermic treatment". *Physics in Medicine and Biology*, 27(11):1301–1311, 1982.
- [36] J. Hardy, A. Gagge, and J. Stolwijk, editors. *Physiological and Behavioral Temperature Regulation*. New York: Thomas, 1970. pp. 281–301, 345–357.
- [37] P. Bard, editor. *Medical Physiology*. St. Louis, Mo.: Mosby, 11 edition, 1961. p. 240.
- [38] H.N. Kritikos, K.R. Foster, and H.P. Schwan. "Temperature profiles in spheres due to electromagnetic heating". *Journal of Microwave Power*, 16(3/4):327–344, 1981.
- [39] WebElements™ Periodic Table. <http://www.webelements.com>, 2000.
- [40] URL: http://www.binternet.com/ms_pages/whitematter.html.
- [41] URL: http://www.binternet.com/ms_pages/greymatter.html.
- [42] T. Saude. *Ocular Anatomy and Physiology*. Blackwell Scientific Publications, Oxford, England, 1993.
- [43] J. Forrester, A. Dick, P. McMeneman, and W. Lee. *The Eye: Basic Sciences in Practice*. W.B Saunders Company, LTD, London, 1996.
- [44] J.E. Dowling. *The Retina: An approachable Part of the Brain*. The Belknap Press of the Harvard University Press, Cambridge, Mass., 1987.
- [45] Q. Li, G. Kang, and O.P. Gandhi. "A thermal model of the human head for exposure to EM fields of cellular telephones". Unpublished report, 1999.